Assessment of Mesh Resolution Requirements for Adaptive High-Order Fluid Structure Interaction Simulations

Vivek Ojha[*], Krzysztof J. Fidkowski[†], and Carlos E. S. Cesnik[‡]

Department of Aerospace Engineering, University of Michigan, Ann Arbor, MI 48109, USA

Nathan A. Wukie[§], and Philip S. Beran[¶]

Air Force Research Laboratory, Wright-Patterson Air Force Base, Ohio, 45433, USA

The paper demonstrates an approach to quantify the spatial and temporal errors arising from mesh motion algorithms in fluid structure interaction simulations. A high-order discontinuous Galerkin formulation of the Navier-Stokes equations is used to simulate the fluid flow. An explicit mapping as given in Persson et al.[1] is used as the primary mesh deformation algorithm. The error estimates for the outputs of interest are evaluated by using an adjoint-weighted residual approach. The mesh motion error analysis is conducted on a two-dimensional uniform free stream flow undergoing analytical mesh motion and a NACA0012 airfoil undergoing prescribed rigid-body motion. Output convergence with adaptive meshing is used to investigate the existence of optimized blending regions for the mesh deformation algorithm. Different mesh generation techniques are also assessed for output convergence using adaptive meshing with output-based and residual-based adaptive indicators. Guidelines for initial mesh generation for steady fluid structure interaction simulations are derived from the two test cases used in this study. A better understanding of the error generated by the mesh motion algorithms is achieved from this work.

I. Introduction

There has been a growing interest in using high-order spatial discretization methods for complex and challenging problems such as free-surface flows and fluid structure interaction (FSI). A common way of simulating such problems involving deformable domains is by using Arbitrary Lagrangian Eulerian (ALE) methods. In the ALE framework, the fluid mesh can move at a velocity different from that of the flow, which is useful for modeling problems in which objects move or deform. The ALE method uses a map between the deforming physical domain and a static reference domain and solves transformed equations on the reference domain.[2] Fluid simulations based on the ALE formulation can use $r-$adaptation to obtain an optimized mesh close to solid boundaries[3] or use a mesh deformation technique to conform the fluid mesh to the moving boundaries. Several mesh deformation methods exist in the literature,[4] which can be classified into two main categories, 1) physical-analogy based techniques and 2) interpolation based techniques. The physical analogy methods[5] consider each edge of the mesh to behave as a spring, which has its own stiffness value. On the other hand, the interpolation based methods compute the movement of grid nodes as a function of boundary nodes, which have no attached physical meaning. Radial basis function interpolation[6] and inverse distance methods[7] are some examples of interpolation-based techniques. An alternative to these methods is the use of an explicit expression for the mapping between the reference and physical domain, as introduced by Persson et al.[1] This paper considers primarily the mesh deformation techniques based on the explicit mapping.

---

[*]Ph.D. Candidate
[†]Associate Professor, AIAA Senior Member
[‡]Clarence L. "Kelly" Johnson Collegiate Professor of Aerospace Engineering, Fellow AIAA
[§]Research Aerospace Engineer, Air Force Research Laboratory, AIAA Member
[¶]Principal Research Aerospace Engineer, Air Force Research Laboratory, AIAA Senior Fellow

American Institute of Aeronautics and Astronautics

Moving mesh nodes to accommodate the deformation at the boundary introduces errors into a fluid simulation. These errors are primarily due to the introduction of mesh velocities and distortion of elements, which lead to accuracy losses. One of the most common errors arises from a non-constant Jacobian of the ALE mapping. By virtue of the state representation in an ALE formulation, a non-constant (and non-polynomial) Jacobian leads to a constant free stream state not being preserved identically. A solution for this inaccuracy, introduced by Lesoinne and Farhat,[8] is known as the Geometric Conservation Law (GCL), which conserves uniform flow by linearizing the mapping from the reference to the physical domain.[9] Other GCL formulations are possible, including ones that use an auxiliary equation to compute corrections to the GCL error.[2]

Output-based adaptation methods applied to high-order FSI simulations, to accurately predict instabilities such as flutter,[10] have shown that the errors arising from the mesh deformation algorithm can play a more important role than the spatial and temporal discretization for accurate evaluation of coupled outputs. The mesh motion errors dominate at lower-order approximations of the state, where the adaptation begins, and hence adaptation occurs in the regions affected by the mesh deformation technique. A large amount of literature exists, which compares the various mesh deformation techniques based on mesh quality of the deformed mesh and computational cost.[4] However, the focus of this work is on the errors generated by the mesh deformation algorithms. Adjoint-based output-error estimates provide a way for quantifying the effect of such mesh deformation errors by relating a specific functional output directly to the local residuals by solving an additional linear problem.

In this paper, a mesh-motion algorithm based on explicit mapping is optimized to reduce mesh-motion errors using error estimates and rates of output convergence. The outline of the remainder of the paper is as follows. Section II reviews the governing equations. Section III reviews the mesh motion algorithm used in this study and the errors generated by such a mesh deformation algorithm, in general. Section IV reviews the output-based error estimation and the mesh adaptation procedure used for the output convergence study. Finally, Section V outlines the results generated using these methods for two separate cases, demonstrating the use of output-based mesh adaptation in efficiently reducing the spatial errors generated by the mesh distortion as well the spatial discretization, thus, showing its applicability to FSI simulations.

II. Governing Equations

II.A. Compressible Flow

The fluid system is governed by the Navier-Stokes equations, given by

$$\left.\frac{\partial \mathbf{u}}{\partial t}\right|_x + \nabla \cdot \vec{\mathbf{F}}(\mathbf{u}, \nabla \mathbf{u}) = \mathbf{0}, \quad \vec{\mathbf{F}} = \vec{\mathbf{F}}^i(\mathbf{u}) - \vec{\mathbf{F}}^\nu(\mathbf{u}, \nabla \mathbf{u}), \tag{1}$$

where $\mathbf{u}(\vec{x}, t) \in \mathbb{R}^s$ is the conservative state vector, $\vec{x} \in \mathbb{R}^d$ is the spatial coordinate, $t \in \mathbb{R}$, and $\vec{\mathbf{F}}^i$ and $\vec{\mathbf{F}}^\nu$ are the inviscid and viscous fluxes, respectively. In the case of a non-deformable domain, the fluid equations are solved numerically in the Eulerian frame of reference, where the computational grid is fixed relative to the fluid. However, numerical simulation of fluid dynamics involving a deforming domain, such as in the case of FSI, faces issues due to the lack of a precise interface definition and under-resolved flow features, when solved in the Eulerian frame of reference. The Lagrangian approach on the other hand, faces problems dealing with large distortions of the computational domain. To resolve these issues, an alternate method, the Arbitrary Lagrangian Eulerian approach, has been introduced and is applied in the present work.

II.B. Arbitrary Lagrangian-Eulerian Formulation

The Arbitrary Lagrangian Eulerian (ALE) approach combines advantages of both the Eulerian and Lagrangian approaches. In this method, the deformable physical domain is mapped to a fixed reference domain by a time-dependent mapping. A simple and effective ALE method for DG was introduced by Persson et al.[2] and a similar approach is followed in this work.[11]

Let the physical space be defined by $v(t)$ and the reference space by V, and let $G(\vec{x}, t)$ represent the one-to-one time-dependent mapping between the two spaces. Each point $\vec{X}$ in the static reference space is mapped

to a corresponding point $\vec{x}(\vec{X}, t)$ in the physical space, based on the desired deformation of the mesh. The gradient of the mapping, represented by $\mathbf{G}$, and the mapping velocity, $\vec{v}_X$, are given by:

$$\mathbf{G} = \nabla_X G, \quad \vec{v}_X = \frac{\partial G}{\partial t}\bigg|_X \tag{2}$$

Let $g = \det(\mathbf{G})$. The corresponding Navier-Stokes equations in the reference frame can be written as[2]

$$\frac{\partial \mathbf{u}_X}{\partial t}\bigg|_X + \nabla_X \cdot \vec{\mathbf{F}}_X(\mathbf{u}_X, \nabla_X \mathbf{u}_X) = \mathbf{0}, \quad \vec{\mathbf{F}}_X = \vec{\mathbf{F}}_X^i(\mathbf{u}_X) - \vec{\mathbf{F}}_X^\nu(\mathbf{u}_X, \nabla_X \mathbf{u}_X), \tag{3}$$

where the transformed vectors, derivatives, and fluxes in the reference frame are given by:

$$\mathbf{u}_X = g\mathbf{u}, \tag{4}$$

$$\nabla_x \mathbf{u} = \nabla_X(g^{-1}\mathbf{u}_X)\mathbf{G}^{-T} = (g^{-1}\nabla_X\mathbf{u}_X - \mathbf{u}_X\nabla_X(g^{-1}))\mathbf{G}^{-T}, \tag{5}$$

$$\vec{\mathbf{F}}_X^i = g\mathbf{G}^{-1}\vec{\mathbf{F}}^i - \mathbf{u}_X\mathbf{G}^{-1}\vec{v}_X, \qquad \vec{\mathbf{F}}_X^\nu = g\mathbf{G}^{-1}\vec{\mathbf{F}}^\nu. \tag{6}$$

II.C. Spatial Discretization

To discretize the state equations (Eq. 3), a discontinuous Galerkin (DG) finite-element method is used in space. DG,[12] as a finite-element method, approximates the state $\mathbf{u}$ in functional form using linear combinations of basis functions on each element. No continuity constraints are imposed between adjacent elements. Denoting by T_h the set of N_e elements in a non-overlapping tessellation of the domain Ω, the state on element e, Ω_e, is approximated as

$$\mathbf{u}_h(\vec{x}(\vec{\xi}))\big|_{\Omega_e} = \sum_{n=1}^{N_p} \mathbf{U}_{en}\phi_{en}(\vec{x}(\vec{\xi})). \tag{7}$$

In this equation, N_p is the number of basis functions per element, $\mathbf{U}_{en}$ is the vector of s coefficients for the nth basis function on element e: $\phi_{en}(\vec{x}(\vec{\xi}))$, and s is the state rank. $\vec{x}$ denotes the global coordinates, and $\vec{\xi}$ denotes the reference-space coordinates in a master element. Formally, $\mathbf{u}_h \in \boldsymbol{\mathcal{V}}_h = [\mathcal{V}_h]^s$, where, if the elements are not curved, $\mathcal{V}_h = \{u \in L_2(\Omega) : u|_{\Omega_e} \in \mathcal{P}^p \ \forall \Omega_e \in T_h\}$, and $\mathcal{P}^p$ denotes polynomials of order p on the element. With the spatial discretization described above, the governing equations can be written in abbreviated form as

$$\bar{\mathbf{R}}_f = \mathbf{M}_f \frac{d\mathbf{U}_f}{dt} - \mathbf{r}_f = \mathbf{0}, \tag{8}$$

where $\mathbf{r}_f$ is the discrete spatial residual vector, $\bar{\mathbf{R}}_f$ is the temporally strong-form unsteady residual, M_f is the mass matrix and the f subscript denotes that these equations apply to the fluids subsystem.

III.   Mesh Deformation

III.A.   Errors Generated by Mesh Deformation

Mesh deformation algorithms generate spatial and temporal errors in a simulation by two main mechanisms. Distortion of the fluid mesh to accommodate the prescribed deformation causes mesh elements to distort. Representing the distorted shape of the elements using linear elements introduces spatial errors in the simulation. These errors exist for both steady and unsteady simulations as they exist in the presence of any deformation of the mesh. For unsteady simulations involving mesh deformation, grid velocities are also introduced in the mesh, which are arbitrary in nature and depend on the mesh motion algorithms. These non-physical mesh velocities introduce spatial and temporal errors in the simulation. The primary focus of this work is to quantify the spatial errors generated only from distortion of mesh elements for a steady fluid simulation on a deformed mesh. A brief analysis of the unsteady mesh motion errors is also discussed for a freestream undergoing mesh deformation.
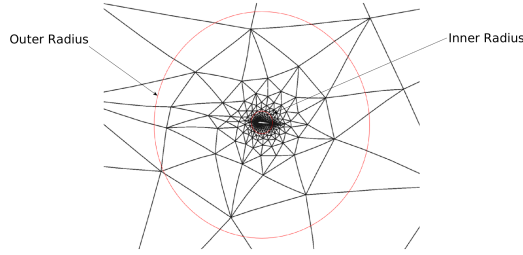
Figure 1. Example of inner and outer radius of the blending region for the explicit mapping mesh motion.

III.B. Explicit Mapping

For deforming domains, the ALE formulation of the Navier-Stokes equations requires a mapping between the reference and the deformed physical mesh. The mapping interpolates the boundary displacements to the interior of the fluid mesh. The explicit mapping presented by Persson et al.[1] does not require solving a system of equations for deforming the volume. It uses explicit expressions for the mapping, which blends the motion, reduces to the identity mapping away from the boundary, and is smooth in-between. For any rigid body deformation, the mesh motion algorithm divides the entire spatial domain into two regions based on inner and outer radii of the blending region. The region extending up to the inner radius from the center of the deformation marks the region of rigid deformation. Within this region, any deformation provided by the user is applied to the all of the mesh elements without any blending. The presence of the rigid region prevents errors such as mesh element inversion in highly-stretched elements, which face such errors when placed in a blending region. The blending region, which exists between the inner and outer radii from the center of the motion, uses a polynomial function to blend the deformation radially such that deformation goes to zero at the outer radius. To achieve blending of the motion, polynomial blending functions $p(r)$ of odd degrees are used. The three different blending polynomials analyzed in this study are cubic, $p(r) = 3r^2 - 2r^3$, quintic, $p(r) = 10r^3 - 15r^4 + 6r^5$ and septic, $p(r) = -20r^7 + 70r^6 - 84r^5 + 35r^4$ where r is the normalized radial distance from the inner radius, respectively. Figure 1 shows the deformed mesh for an airfoil undergoing rigid-body pitch motion. The inner and outer radii are placed at one and ten chords away from the center of motion, which is at the quarter chord of the airfoil.

IV. Output-Based Mesh Adaptation

In fluid simulations involving deforming domains, the numerical error in the output results from discretization errors and mesh motion errors. To evaluate the error estimates on the output of interest, spatially discrete but continuous in time adjoints are used.[13] For schemes employing a finite-dimensional polynomial basis in space and time, numerical errors pollute the calculations of the state and quantities of interest. Fundamentally, the errors are caused by approximations inherent to the spatial and temporal discretization. Mesh deformation magnifies these errors, due to warping of the domain. This effect manifests itself in part in the loss of conservation, as discussed in Section I, but even with GCL, deformation errors persist in higher moments of the solution. That is, the implementation of the GCL reduces conservation errors but does not eliminate all the errors arising due to mesh motion, such as non-physical mesh velocity and distortion of the elements. Output-based error estimates give a better quantification of the contribution of errors from mesh motion for the desired outputs. The GCL is not enforced in this study, and instead, the management of mesh motion errors is left to the output-based error estimates.

IV.A. Continuous-in-Time Adjoint Evaluation

Consider an unsteady output of the form

$$\bar{J} = \int_0^{\mathrm{T}} J(\mathbf{U}_f, t) \ dt, \tag{9}$$

where J is a spatial functional of the fluid, $\mathbf{U}_f$, state. The continuous adjoint, $\mathbf{\Psi}_f$, represents the sensitivity of the output to perturbations in the unsteady residuals $\bar{\mathbf{R}}_f$. To derive the adjoint equations, a Lagrangian is defined as

$$\mathcal{L} = \bar{J} + \int_0^{\mathrm{T}} \mathbf{\Psi}_f^T \bar{\mathbf{R}}_f dt. \tag{10}$$

Substituting Eq. 9 into Eq. 10, integrating the second term by parts and requiring stationarity of the Lagrangian with respect to the permissible state variations, which in this particular work is only in the fluid state, $\delta \mathbf{U}^f$, gives

$$\mathbf{\Psi}_f^T \mathbf{M}_f \delta \mathbf{U}_f \Big|_{t=\mathrm{T}} - \mathbf{\Psi}_f^T \mathbf{M}_f \delta \mathbf{U}_f \Big|_{t=0} + \int_0^{\mathrm{T}} \left[\frac{\partial J}{\partial \mathbf{U}_f} - \frac{\mathrm{d}\mathbf{\Psi}_f^T}{\mathrm{d}t} \mathbf{M}_f - \mathbf{\Psi}_f^T \frac{\partial \mathbf{r}_f}{\partial \mathbf{U}_f} \right] \delta \mathbf{U}_f dt = 0. \tag{11}$$

The middle term at $t = 0$ drops out since the initial condition on the primal fully constrains the state there, so $\delta \mathbf{U}^f = 0$ at $t = 0$. The remaining terms yield the adjoint differential equation (from the time integrand, transposed),

$$-\mathbf{M}_f \frac{\mathrm{d}\mathbf{\Psi}_f}{\mathrm{d}t} - \frac{\partial \mathbf{r}_f^T}{\partial \mathbf{U}_f} \mathbf{\Psi}_f + \frac{\partial J^T}{\partial \mathbf{U}_f} = \mathbf{0}, \tag{12}$$

and the terminal condition

$$\mathbf{\Psi}_f(\mathrm{T}) = \mathbf{0}. \tag{13}$$

Due to the terminal condition, the adjoint equation is solved backward in time. The time integration scheme used for both the primal and the adjoint equation for this study is ESDIRK4, but other time schemes can be used as well.

IV.B. Error Estimation

The unsteady adjoint can be used to evaluate the error in the output of interest through the adjoint-weighted residual.[14] Let $\mathbf{U}_H^f$ be the approximate fluid solution obtained from the current space-time discretization denoted by subscript H and $\bar{\mathbf{\Psi}}_{f,h}^T$ be the fluid adjoint in the fine space denoted by h. The error in the output is defined as:

$$\delta J = J_H(\mathbf{U}_{f,H}) - J_h(\mathbf{U}_{f,h}) \approx \frac{\partial J_h}{\partial \mathbf{U}_{f,h}} \delta \mathbf{U}_{f,h} \approx -\int_0^T \mathbf{\Psi}_{f,h}^T \bar{\mathbf{R}}_{f,h}(\mathbf{U}_{f,H}) dt, \tag{14}$$

where $\delta \mathbf{U}_{f,h} = \mathbf{U}_{f,h}^H - \mathbf{U}_{f,h}$ is the primal error in the fluid state and $\mathbf{U}_{f,h}^H$ is the injected solution from space H to h. The exact unsteady adjoint, which is unavailable, is approximated in a finer space by increasing the degrees of freedom in the spatial and temporal discretizations.

IV.C. Mesh Adaptation

Error estimates in the space-time fluid mesh guide the adaptation process. Space-time elements selected for refinement or coarsening are decided by two factors: 1) estimated error in the space-time element, 2) computational cost of refinement. These two aspects are combined into an adaptive indicator called the "figure of merit", which is the element error eliminated by refinement divided by the degrees of freedom introduced by the refinement. A growth factor, specified by the user, defines the degrees of freedom added after each adaptation cycle. The adaptive strategy used in this work refines in space by spatial order refinement (p-adaptation). However, h-adaptation is also used to generate some of the initial meshes before p-adaptation.

V. Results

In this section, the impact of mesh motion algorithms on a high-fidelity fluid simulation with deforming domains is studied on an unstructured mesh. Two separate cases have been designed for quantifying and analyzing the errors arising from mesh deformation. Firstly, a free stream preservation test, which is widely

used for highlighting the impact of non-linear mapping in a free stream is modified to quantify the errors generated by the mesh deformation. In this case, the impact of the mesh deformation is characterized by entropy generation. Secondly, a more practical case of an airfoil undergoing rigid body deformation in a steady fluid flow is analyzed for engineering outputs of interest such as lift.

V.A. Free-stream preservation

Spatial and temporal errors generated in a fluid simulation with deforming domains arise from the corresponding space-time discretization and mesh deformation. As both sources of error propagate spatially and temporally in a simulation, it is difficult to separate the errors obtained from the output-based error estimate based on the source. However, for an arbitrary mesh motion applied to a free stream, the states are only contaminated by the errors arising from mesh deformation, as the space-time discretization without deformation conserves the free stream. Therefore, such a test acts as an ideal case to study the spatial and temporal distribution of mesh deformation errors. A steady and an unsteady mesh motion error quantification study are presented for a freestream undergoing mesh deformation. Error estimates on the entropy generated by the mesh deformation are used to demonstrate the existence of optimum blending region for the mesh motion algorithm.

Consider a uniform fluid flow around an airfoil placed centrally in square domain which spans $[-100c, 100c]$ in both dimensions, where c is the chord length of the airfoil. To simulate a uniform fluid flow, a coarse, unstructured, triangular mesh of 5489 elements is generated, as shown in Figure 2. The unstructured triangular fluid meshes used in this paper are generated using BAMG,[15] an anisotropic 2D mesh generator. For fixed, user defined, degrees of freedom, BAMG is used to generate an h-adapted mesh, optimized using metric-based mesh adaptation. Freestream boundary conditions are applied at the far away boundaries as well as on the airfoil. The airfoil boundary acts as the set of the nodes where the deformation is prescribed but as the boundary condition on the airfoil is free-stream it does not violate the preservation phenomenon that it is setup for. Despite this being a free-stream preservation test, the reason for choosing a viscous mesh is because most of the instabilities that occur in FSI simulations, such as flutter, occur at high Reynolds number flows. Thus, a mesh capable of simulating such as system is used to study the impact of 'otion. Two degrees of freedom of the airfoil motion i.e the pitch, $\alpha(t)$ and plunge, $h(t)$, are prescribed using sinusoidal functions. An explicit mesh deformation algorithm, as mentioned in Section III, is applied to handle the deformations occurring in the fluid domain due to the moving airfoil. The mesh deformation algorithm, is dependent on three variables i.e, the inner radius, the outer radius, and the polynomial blending function, which are generally user-defined. However, as shown in the work by Ojha et al.,[10] the blending region is

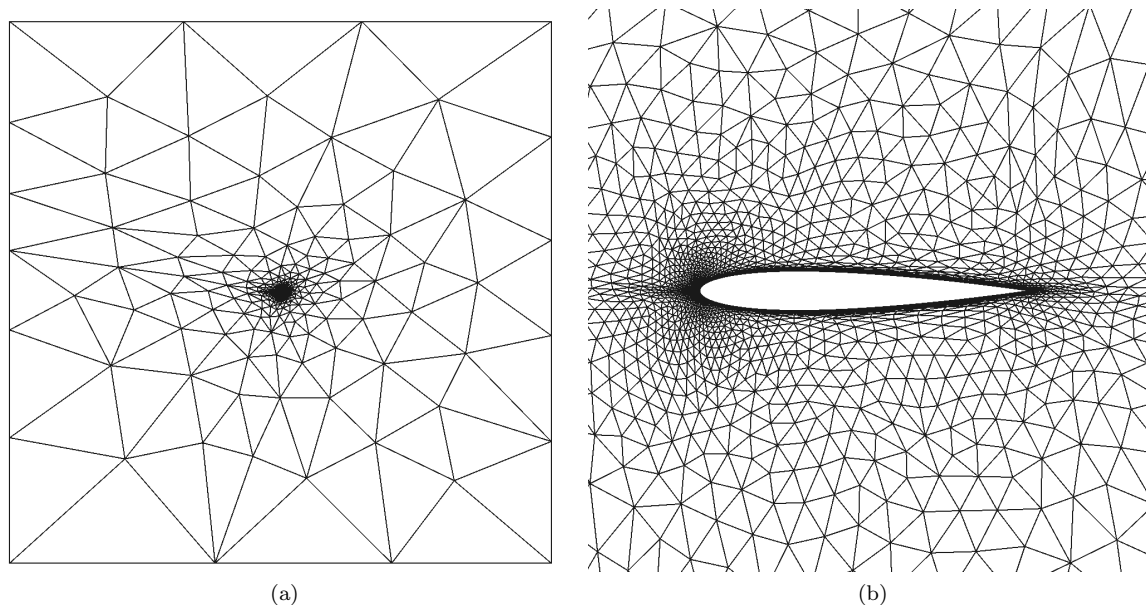<div align="center">(a)</div>
<div align="center">(b)</div>

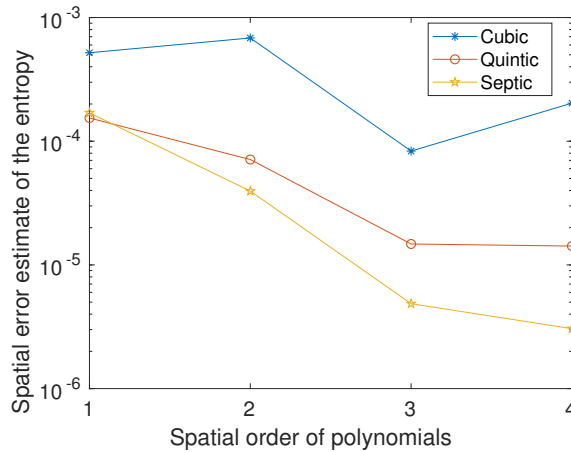**Figure 2. Unstructured viscous mesh for the free-stream preservation test.**

Figure 3. Effect of the order of the blending polynomial on the error estimate.

important in an adaptive FSI problem. Thus, a study is conducted to investigate the existence of an optimal blending region and blending function for a viscous mesh undergoing arbitrary motion, with the goal of minimizing the error due to mesh deformation.

The optimum region is evaluated for both steady and unsteady cases. For the steady-state deformation, an inviscid simulation is conducted with $p = 3$ order polynomials with a constant pitch deformation of 5 degrees, centered at the quarter chord of the airfoil. The error estimate for the steady case is evaluated for an output defined as the domain integral of the entropy, given by

$$\bar{J} = \int_{\Omega} E d\Omega. \tag{15}$$

Figure 3 compares the effect of order of blending polynomials on the entropy error estimate for inner and outer radii of $1c$ and $5c$. It shows that across different orders of dicretizations, increasing the order of blending polynomials leads to better representation of the deformation in the elements, which in turn leads to lower errors, provided a sufficiently high quadrature rule is used for integration when mesh motion is active. Figure 4a shows a contour representation of error estimates for varying inner and outer radii of the blending region with septic blending. The optimum inner and outer radii for the lowest error estimate come out to be $1c$ and $5c$, respectively. We can conclude that lowering the inner radius to be as low as possible while avoiding element inversion reduces the errors in the output due to mesh motion, because this results in a blending region located in the domain which is finer. Lowering the outer radius causes the blending to occur in a very small domain resulting in large gradients within the elements thereby causing higher errors. Similarly, increasing the outer radius of the blending region also results in an increase in the error because the number of elements affected by the blending region grows, as does the size of these elements. For this case, the optimum outer radius was identified at $5c$, which lies between the two extremes and leads to the lowest errors arising from mesh motion. The optimum parameters are specific to the case tested. However, similar results are expected for the blending region location for viscous meshes i.e, close to the deforming domain for the least mesh motion errors. Similar optimum blending region is also observed for different amplitude of the deformation in other degrees of freedom. Apart from error estimates, the actual error in the average entropy in the entire domain is also studied for varying outer radii, as shown in Figure 4b, which depicts a similar behaviour as the error estimate.

To study the propagation of spatial and temporal error arsing due to mesh motion, an unsteady pitch motion was prescribed to the fluid system given by $\alpha = \alpha_0 \sin(t)$ where $\alpha_0 = 5°$. The inviscid simulation was conducted with $p = 3$ and $p = 4$ order polynomials and an ESDIRK4 time scheme with 50 time steps for a final time of 5 time units, where one time unit is the convective time unit defined as the time taken for flow at free-stream speed to traverse the chord of the airfoil. The output chosen for the unsteady adjoint evaluation and error estimate is the domain integral of the entropy at the final time. Figure 5 shows the
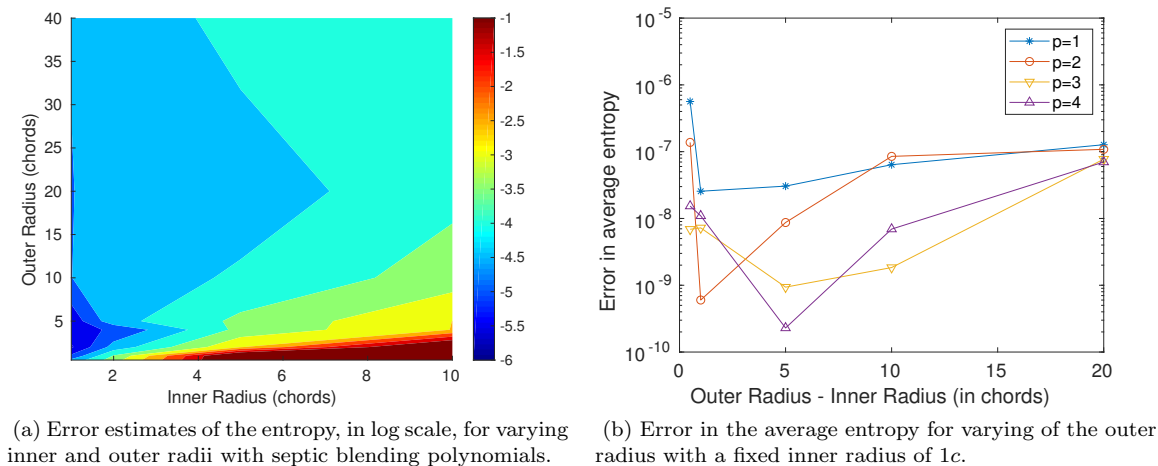
(a) Error estimates of the entropy, in log scale, for varying inner and outer radii with septic blending polynomials.

(b) Error in the average entropy for varying of the outer radius with a fixed inner radius of $1c$.

Figure 4. Error and error estimates of the entropy

evolution of spatial error estimates over time for $p = 4$ for varying outer radii with a constant inner radius of $1c$ and septic blending. The results from the steady state are corroborated with the unsteady solution where a similar optimum and outer radius is observed to reduce the error estimate.

V.B. NACA 0012 airfoil with prescribed pitch deformation

The second case test case is designed to study the effect of mesh motion errors on more practical problems, with an engineering output of interest. In this problem, mesh deformation is applied to an airfoil with pre-scribed rigid-body motion and the output of interest chosen for the study is the lift generated by the airfoil. The investigation is conducted for both viscous and inviscid flows. The main motivation behind this problem is to investigate the effect of the position of blending regions on the convergence of the output of interest. Secondly, a comparative study based on the effect of the initial mesh used for simulation undergoing mesh deformation is also performed for three separate initial meshes. Finally, the effect of different definitions of error estimates used for mesh adaption on the output convergence is also investigated for simulations undergoing mesh deformation.

Consider a NACA 0012 airfoil placed centrally in a circular mesh of radius 1000 chords. A pitch deformation of five degrees about the leading edge is provided to the airfoil using the mesh motion algorithm described in Section III. The effect of viscosity on the mesh deformation error is studied by considering two
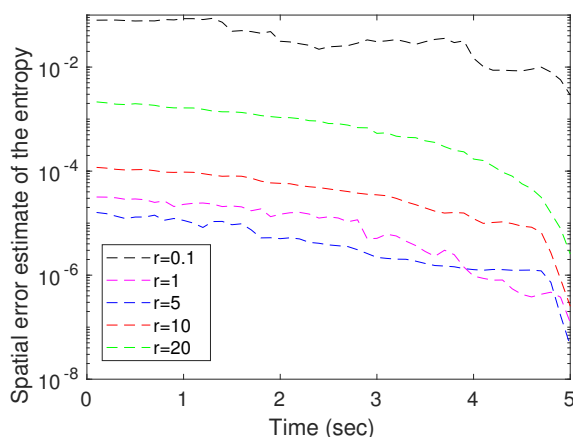

Figure 5. Unsteady spatial error estimate of the entropy for varying outer radii with an inner radii of $1c$ and septic blending polynomials

American Institute of Aeronautics and Astronautics

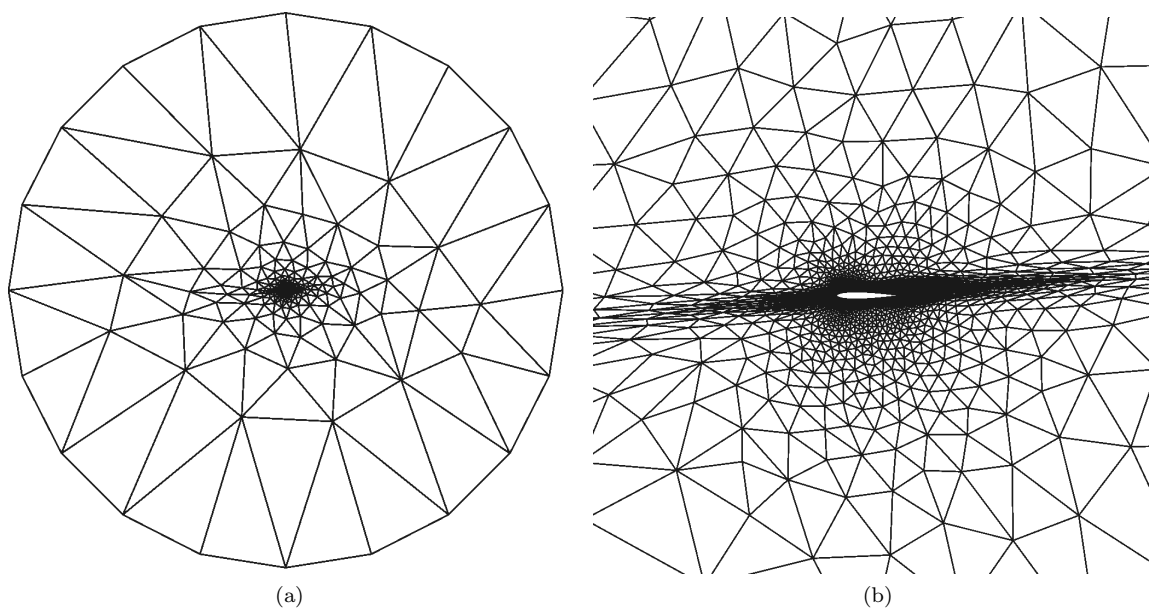Cleared for Public Release on 8 November 2019. Case Number: 88ABW-2019-5482.

Figure 6. Reference mesh for lift evaluation for laminar flow.

flow conditions, viscous and inviscid flow. For the viscous simulations, the Reynolds number is chosen to be Re=1000. The focus of this analysis is to quantify only the spatial errors generated by distortion of the mesh elements by the mesh motion algorithm. Therefore, all the simulations are steady in nature. The meshes used for this simulation use curved elements of order three, q=3, to represent the airfoil geometry. Freestream boundary conditions are applied at the farfield boundaries and wall boundary conditions are applied at the airfoil boundary. The Mach number used for this analysis is M=0.345.

Multiple inner and outer radii combinations are used to vary the position of the blending region for the deformation to study the effect of the position of the blending region on the output convergence. For a particular blending region, the spatial errors in the simulation are quantified by comparing the output of interest against a reference case, which is unaffected by mesh motion. In the reference case, the desired angle of attack is achieved by changing the flow boundary conditions at the farfield without applying any
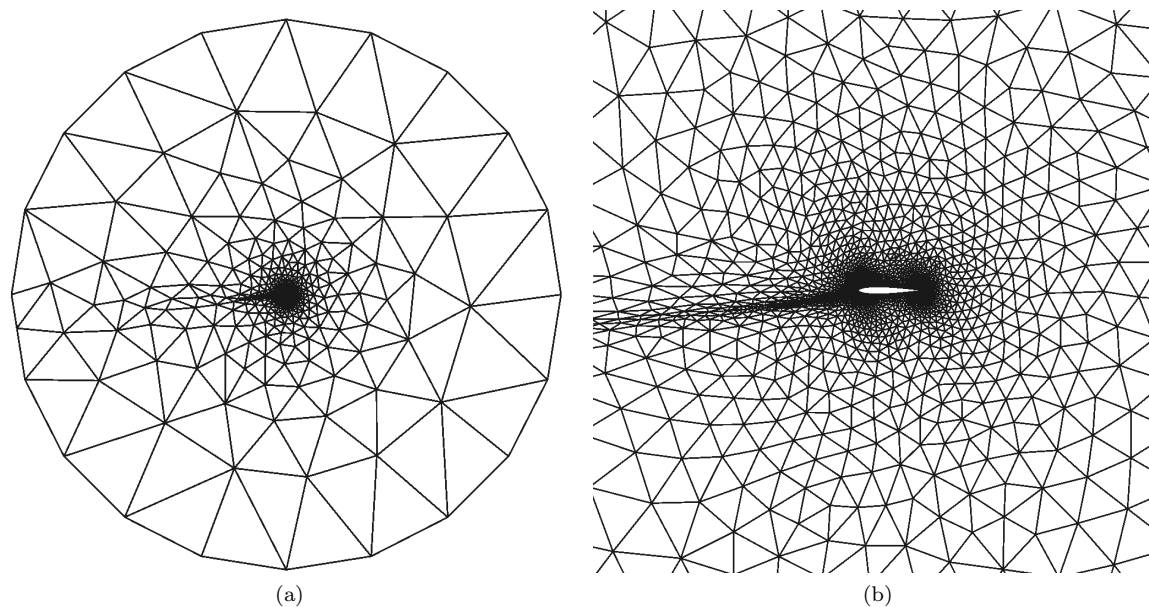

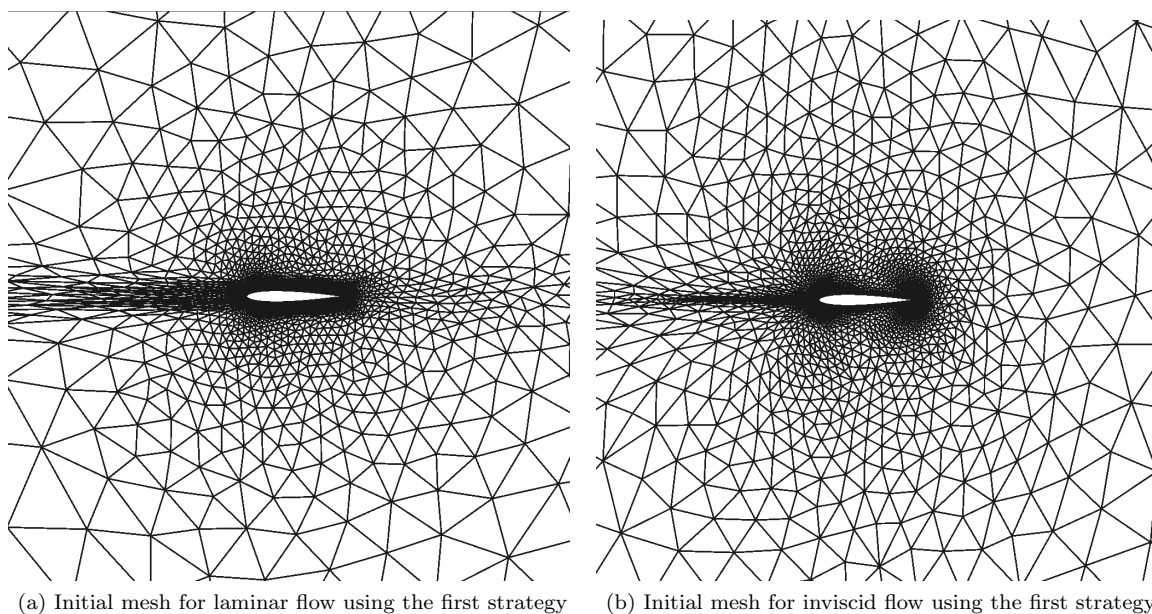**Figure 7. Reference mesh for lift evaluation for inviscid flow.**

American Institute of Aeronautics and Astronautics
Cleared for Public Release on 8 November 2019. Case Number: 88ABW-2019-5482.

(a) Initial mesh for laminar flow using the first strategy   (b) Initial mesh for inviscid flow using the first strategy

Figure 8. Initial mesh optimized for the reference position of the airfoil in ALE.

mesh deformation to the airfoil. Figure 6 and Figure 7 present the meshes used for the laminar and inviscid reference cases, respectively. The reference lift is evaluated for a spatial discretization of order five, $p = 5$ using the mesh of around 5000 elements. Using an initial mesh optimized for the flow configuration leads to better output convergence. However, for simulations involving mesh deformation, where the deformation may or may not be known to the user before the simulation, different initial meshes can lead to varied output convergence. Therefore, for the prescribed mesh deformation on an airfoil, three strategies on generating these initial meshes are analyzed based on output convergence. The three strategies are described below.

V.B.1.   Mesh optimized for the reference position of the airfoil in ALE

Simulations involving mesh deformation generally use a mesh optimized for the reference position in ALE as the initial mesh. In simulations involving FSI, the mesh deformation is often not known apriori to the user. Therefore, this strategy is useful as it is optimized to reduce spatial discretization errors and can yield a good initial mesh. Using this strategy, a mesh optimized for the reference position of the airfoil in the ALE framework, where the airfoil is aligned with the flow is obtained, as shown in Figure 8. Employing such a mesh h optimized without mesh motion can lead to different output error, depending on the mesh motion algorithm itself. Starting with this initial mesh, the mesh motion algorithm deforms the mesh for the various combination of inner and outer radii. For the error analysis, discrete values of inner radius, $R_{\text{inner}} \in [1c, 5c, 20c, 40c, 100c]$ and blending distance, which is the distance between the inner and outer radius, $D_{\text{blending}} \in [1c, 5c, 20c, 40c, 100c, 400c, 800c]$, are used. As a single mesh is used for the error estimation for the various blending region, the initial spatial error arising only from the discretization is the same for all the blending regions. To study the effect of the mesh deformation, an output convergence study is conducted using output based mesh adaptation. Starting with uniform $p = 1$ elements in the entire domain, the initial mesh is adapted in spatial order by subjecting it to six cycles of p-adaptation. The growth factor is chosen to be two for each adaptation cycle.

Figure 13 and Figure 16 show the output convergence for the different blending regions as a function of the adaptive iteration for the laminar and inviscid flows respectively. The various plots track the error in lift for a constant inner radius and varying outer radius. As the convergence of lift is not a monotonic function of the adaptive iteration, the sudden drop in the error of the output is not an indication of convergence but a sign of the output crossing the reference lift en route to convergence. The existence of two optimum blending regions can be observed from Figure 9a, which shows the error in the lift at the end of the adaptive iterations for laminar flow. The first optimum blending region is located close to the airfoil. This location of the blending region benefits from the mesh density of the initial mesh used for the simulations. The initial
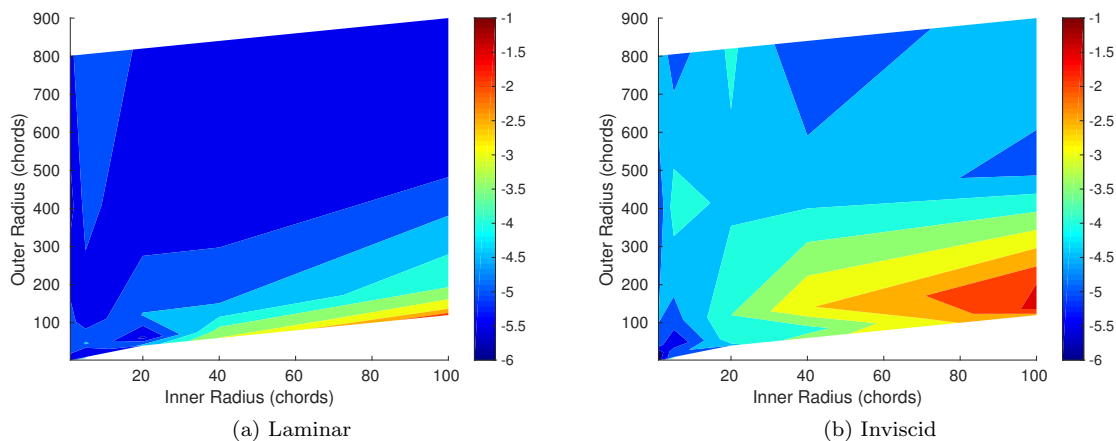
American Institute of Aeronautics and Astronautics
Cleared for Public Release on 8 November 2019. Case Number: 88ABW-2019-5482.

(a) Laminar

(b) Inviscid

Figure 9. Error in lift post output-based adaptation using the initial meshes proposed in the first strategy.

mesh optimized for the reference position leads to a finer mesh close to the airfoil, which effectively resolves the boundary layer. Similarly, lack of flow features far away from the airfoil result in larger element sizes there. Due to a finer mesh close to the airfoil, the blending region is well-resolved and leads to less distortion within each element, thereby resulting in better output convergence. The second optimum blending region exists where the outer radius extends far away from the airfoil. Irrespective of the inner radius, having a larger outer radius results in less distortion within an element, which in turn results in less mesh deformation error. Relatively slow convergence can be seen in the output for cases having small blending regions with larger inner radius. Pushing the inner radius away from the airfoil and keeping the blending region small results in the blending occurring primarily in elements of larger sizes. These large elements are incapable of resolving the blending well, thus leading to high errors. Similar optimum blending regions are observed for the inviscid case as well, as shown in Figure 9b. For the inviscid case, the optimum blending region close to the airfoil outperforms the optimum blending region away from the airfoil due to the initial mesh used for the inviscid flow. The initial optimized mesh for the inviscid case is more isotropic compared to the viscous flow case because of the lack of the boundary layer. The isotropic nature of the mesh combined with the radial nature of the blending leads to a better resolution for the deformations blended close to the airfoil.

The output convergence study in this analysis is conducted using output-based mesh adaptation. This technique is successful in targeting the elements in the blending region for further adaptation because of the definition of the adaptive indicator. As described in Section IV, the adaptive indicator is a function of the adjoint and the residual evaluated by projecting the coarse space solution into the fine space. The elements inside the blending region, despite having a lower adjoint magnitude suffer from the errors originating from
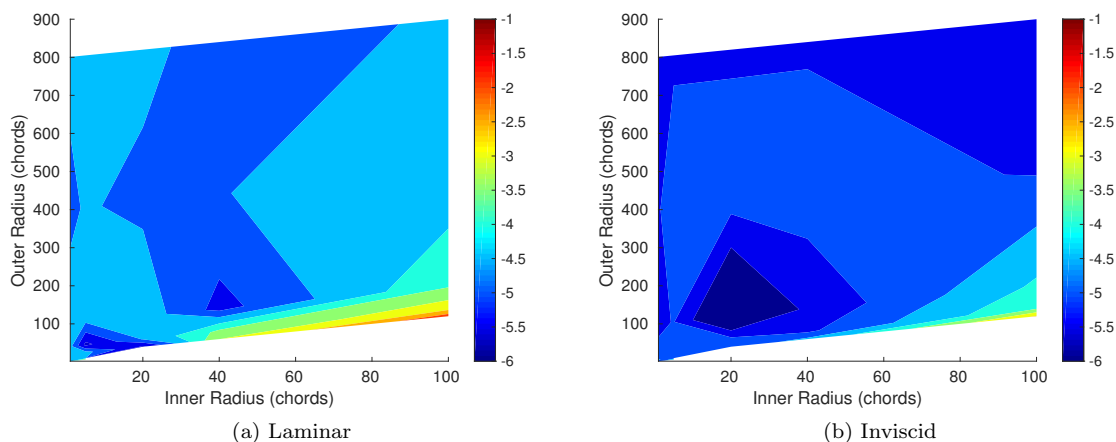

(a) Laminar

(b) Inviscid

Figure 10. Error in lift post residual-based adaptation using the initial meshes proposed in the first strategy.

American Institute of Aeronautics and Astronautics

Cleared for Public Release on 8 November 2019. Case Number: 88ABW-2019-5482.

mesh motion and have a higher projected residual. A second definition of the adaptive indicator, based solely on the residual is also tested for output convergence. Figure 10 shows the output convergence for the various blending regions as a function of the adaptive iteration, using residual-based adaptation. The output convergence for the various positions for the blending region in the laminar case is slower for residual-based adaptation when comparing it against output-based adaptation. The inclusion of the lift adjoint in the adaptive indicator focuses the adaptation on mesh elements important for lift evaluation irrespective of the mesh deformation errors. Residual-based adaptation, on the other hand, focuses more on the errors due to mesh deformation in the bigger elements leading to slower convergence. However, the opposite behavior is seen in the case of inviscid flow, where better convergence rates are seen with residual based adaptation. In output-based adaptation, the singularity of the adjoint along the stagnation streamline[16] leads to numerical noise in the adjoint evaluation. This causes excessive adaptation along the stagnation streamline, which is avoided in the case of residual-based adaptation, leading to more efficient output convergence.

Mesh adaptation using residual-based adaptive indicators is comparatively much faster than output-based adaptive indicators due to the lack of the adjoint evaluation. It is also able to highlight some of the shortcomings of the output-based approach, where errors in adjoint evaluations can lead to slower output convergence for inviscid cases. However, such a definition of the error estimate is not useful for unsteady cases, where the information of characteristics, provided by the adjoint, is extremely useful.

V.B.2. *Mesh optimized for the deformed position of the airfoil in ALE*

A second strategy for the initial mesh generation can be used when the mesh deformation is known a priori to the user such as simulations involving prescribed motion to the airfoil. In this strategy, an optimized initial mesh is generated for each specific blending region by taking the known pitch deformation of the airfoil into account. The meshes generated by BAMG for the various blending regions have the same degrees of freedom. Thus, the total spatial error, which is a combination of both the spatial discretization and the mesh deformation, among the various initial meshes is nearly the same. A similar output convergence study using mesh adaptation as described in Section V.B.1, using the new initial meshes, is conducted for the two flow regimes. Figure 14 and Figure 17 show the output convergence for the different blending regions as a function of the adaptive iteration for the laminar and inviscid flow, respectively. The various blending regions show similar rates of output convergence, which can be clearly observed in Figure 11. The contour plot does not show the existence of any optimum blending region for such initial meshes, which is due to the way the initial meshes are generated for these cases. Total spatial errors in the initial meshes are partitioned between the spatial discretization error and the mesh motion error in such a manner by the h-adaptation to give a constant spatial error. For the cases where the mesh deformation errors are dominant, the h-adaptation distributes more degrees of freedom in the blending region and vice-versa for the case with dominant spatial discretization. As the output-based mesh adaptation cannot distinguish between the two sources of spatial errors it reduces both of them at the same rate without any bias resulting in similar output convergence
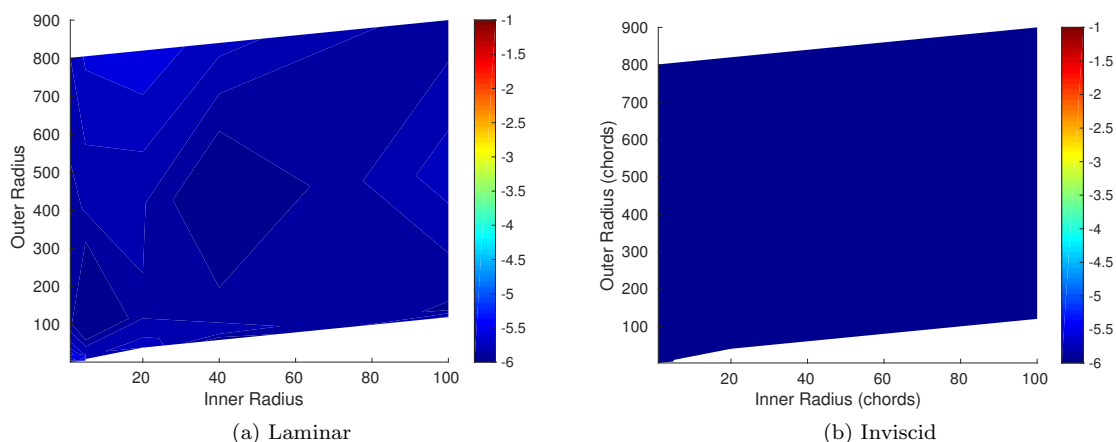

(a) Laminar (b) Inviscid

Figure 11. Error in lift post output-based adaptation using the initial meshes proposed in the second strategy.
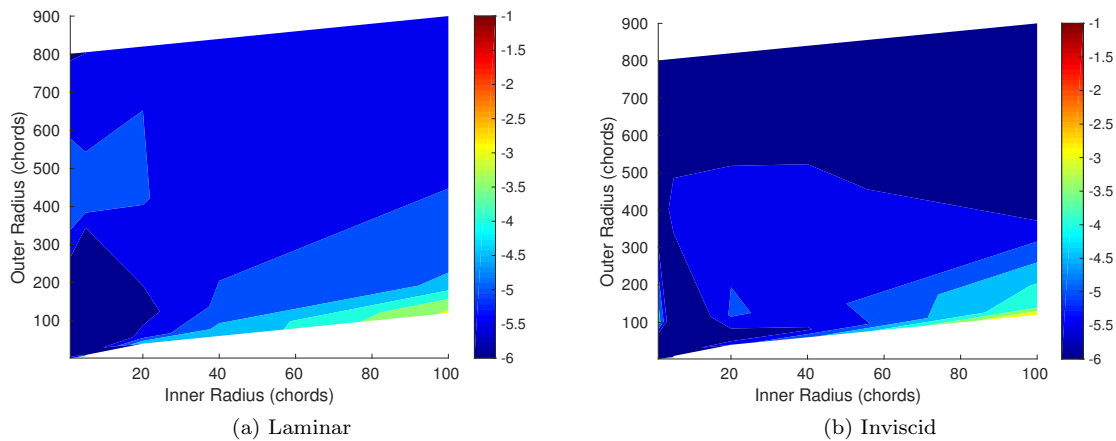
(a) Laminar   (b) Inviscid

Figure 12. Error in lift post output-based adaptation using the initial meshes proposed in the third strategy.

for the various blending regions. This is one of the key advantages of using output-based adaptation for problems with mesh motion.

Comparing the two strategies discussed above, the initial meshes for the second strategy have better rates of convergence than the first strategy for any position of the blending region. While both the strategies use initial meshes with similar total spatial errors, inclusion of the mesh deformation adds additional error in the meshes optimized for the reference position, thereby leading to slower error convergence. Thus, for cases where the mesh deformation is known a priori, using an initial mesh optimized for the blending region leads to better convergence.

V.B.3. *Mesh optimized for the reference lift evaluation of the airfoil*

Meshes used for the reference lift evaluation, where the boundary condition at the farfield is changed to achieve the desired angle of attack, can also serve as good initial meshes for this analysis. Despite, the degrees of freedom used to resolve the wake and regions near the stagnation streamline being aligned differently than the flow direction used in the error analysis, the application of mesh deformation to these meshes re-aligns these regions. Thus, this strategy uses an initial mesh optimized for reducing the spatial discretization errors for the known deformation without knowledge of the blending region. A similar output convergence study using mesh adaptation as described in the previous subsection using the new initial mesh is conducted for the two flow regimes. Figure 15 and Figure 18 show the output convergence for the different blending regions as a function of the adaptive iteration for the laminar and inviscid flow, respectively. The existence of an optimum blending region can be observed from Figure 12a, which shows the error in the lift at the end of the adaptive iterations, for the laminar flow. The optimum blending region is located for small inner radii with an outer radius of 100 chords. For the laminar case, the initial mesh has higher mesh density along the stagnation streamline and the boundary layer. However, the entire stagnation streamline which extends up to the upstream farfield at 1000 chords is not resolved because of the constraint on the total degrees of freedom. Thus, for the given constraint of 5000 elements, the mesh generator only resolves the stagnation streamline up to 100 chords, which makes the blending region with an outer radius of 100c converge more aggressively compared to other locations. Depending on the total degrees of freedom in the initial mesh, the optimum blending region may move further upstream of the airfoil if the stagnation streamline is further resolved. Therefore, the optimum blending region observed for this case is unique to this particular initial mesh, but this study highlights the importance of the initial mesh structure on output convergence for FSI simulations. The inviscid reference mesh, on the other hand, has quite a different distribution of mesh elements compared to the laminar flow mesh. The lack of a boundary layer leads to more isotropic distribution of mesh elements and leads to smaller elements compared to the laminar case in the farfield. Thus, two optimum blending regions are observed for the inviscid case, as seen in Figure 12b. The location of the optimum regions is similar to the first strategy, the explanation of which can be extended to this case as well.

VI.   Conclusions

In this paper, output-based error estimation is applied to fluid simulations on deformed domains. A two-dimensional free-stream preservation test in an inviscid flow is used to quantify error due to mesh-motion algorithms. An output-based error estimate on the entropy norm over the domain gives an estimate of the error due to the mesh deformation procedure. The error estimate is used to optimize the mesh motion algorithm by optimizing the variables used to blend the deformation. For an explicit mapping, an optimized inner and outer radius of the blending is obtained for a steady and unsteady deformation resulting in the least error in the output. A secondary case of an airfoil undergoing rigid body deformation in a steady fluid flow is analyzed to observe the effects of the position of the blending region on the output convergence. The output convergence study verifies that the implementation of a GCL is not necessary for achieving high accuracy in high-order FSI simulations involving rigid body motions. Two different adaptive indicators are also studied and compared for mesh adaptation. While output-based mesh adaptation outperforms residual-based adaptation, the latter highlights some of the shortcomings of the output-based adaptation techniques in the inviscid flow regime. Guidelines for initial mesh generation for steady FSI simulations are derived from the two test cases used in this study. When dealing with mesh deformation, the four significant conclusions from this study are:

1. Deforming the mesh in regions where the mesh density is high is favorable for output convergence

2. Large gradients in deformation occurring within an element are difficult to resolve and should be avoided, especially if the element size is large. Thus, having a blending region extend up to the farfield promotes good convergence and lower gradients within an element.

3. Incorporating mesh deformation in the initial mesh generation process gives better output convergence.

4. Using output-based adaptation leads to balanced errors from mesh motion and the discretization.

These guidelines can also be applied to other mesh motion algorithms with a user defined blending region to achieve low mesh motion errors and better output convergence. A better understanding of the error generated by the mesh motion algorithms is achieved from this work. The two cases presented in this work have been able to demonstrate the use of output-based mesh adaptation in efficiently reducing the spatial errors generated by the mesh distortion as well the spatial discretization, thus, showing its applicability to FSI simulations. The effect of the distribution of elements in the initial mesh on the output convergence is highlighted for high-order FSI simulations. Similar mesh motion error analysis on more complex deformations for unsteady cases with spatial and temporal mesh motion errors are areas where further research is ongoing.

Acknowledgments

References

[1]Persson, P.-O., Peraire, J., and Bonet, J., "A high order discontinuous Galerkin method for fluid-structure interaction," *18th AIAA Computational Fluid Dynamics Conference*, 2007, p. 4327.

[2]Persson, P.-O., Bonet, J., and Peraire, J., "Discontinuous Galerkin solution of the Navier–Stokes equations on deformable domains," *Computer Methods in Applied Mechanics and Engineering*, Vol. 198, No. 17-20, 2009, pp. 1585–1595.

[3]Budd, C. J., Huang, W., and Russell, R. D., "Adaptivity with moving grids," *Acta Numerica*, Vol. 18, 2009, pp. 111–241.

[4]Selim, M., Koomullil, R., et al., "Mesh deformation approaches–a survey," *Journal of Physical Mathematics*, Vol. 7, No. 2, 2016.

[5]Batina, J. T., "Unsteady Euler airfoil solutions using unstructured dynamic meshes," *AIAA Journal*, Vol. 28, No. 8, 1990, pp. 1381–1388.

[6]Kedward, L., Allen, C. B., and Rendall, T. C., "Efficient and exact mesh deformation using multiscale RBF interpolation," *Journal of Computational Physics*, Vol. 345, 2017, pp. 732–751.

[7]Witteveen, J., "Explicit and robust inverse distance weighting mesh deformation for CFD," *48th AIAA Aerospace Sciences Meeting Including the New Horizons Forum and Aerospace Exposition*, 2010, p. 165.

[8]Lesoinne, M. and Farhat, C., "Geometric conservation laws for aeroelastic computations using unstructured dynamic meshes," *12th Computational Fluid Dynamics Conference*, 1995, p. 1709.
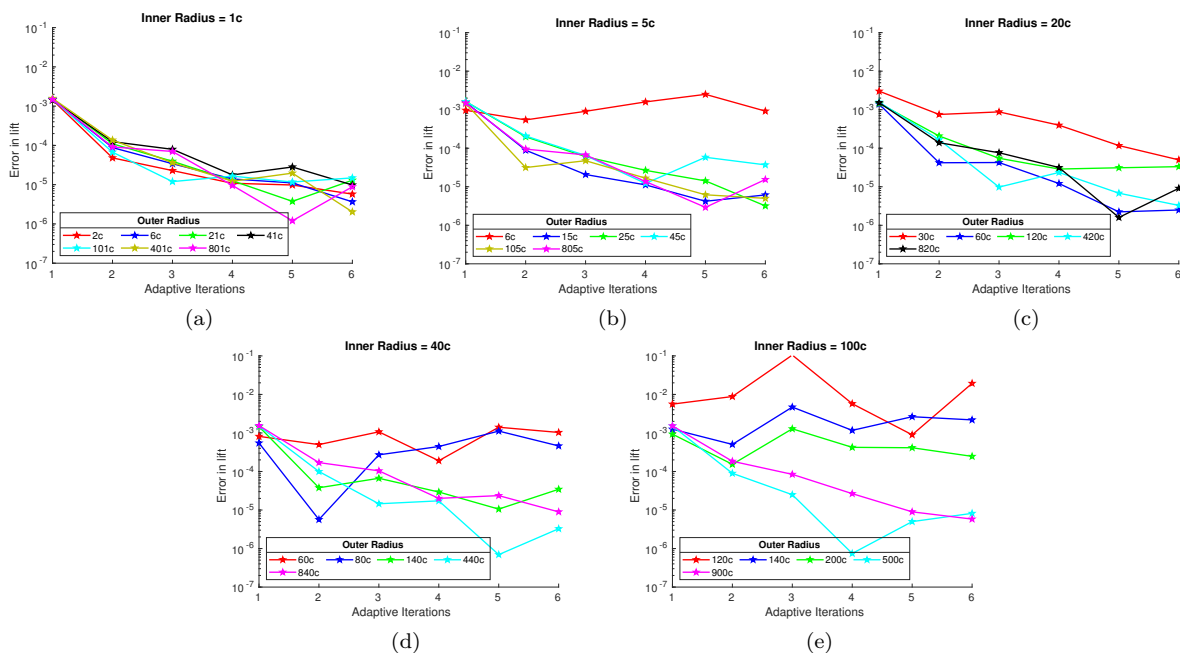
Figure 13. Error in lift generated by the airfoil in a laminar flow as a function of the adaptive iterations for the first mesh adaptation strategy
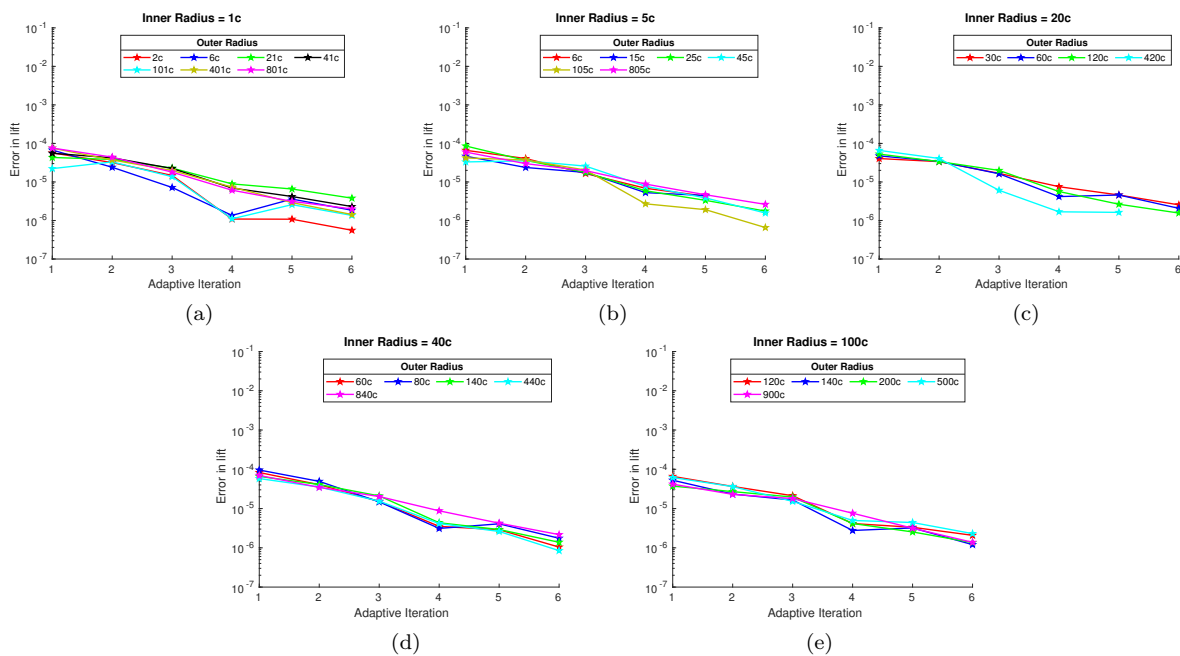

Figure 14. Error in lift generated by the airfoil in a laminar flow as a function of the adaptive iterations for the second mesh adaptation strategy.
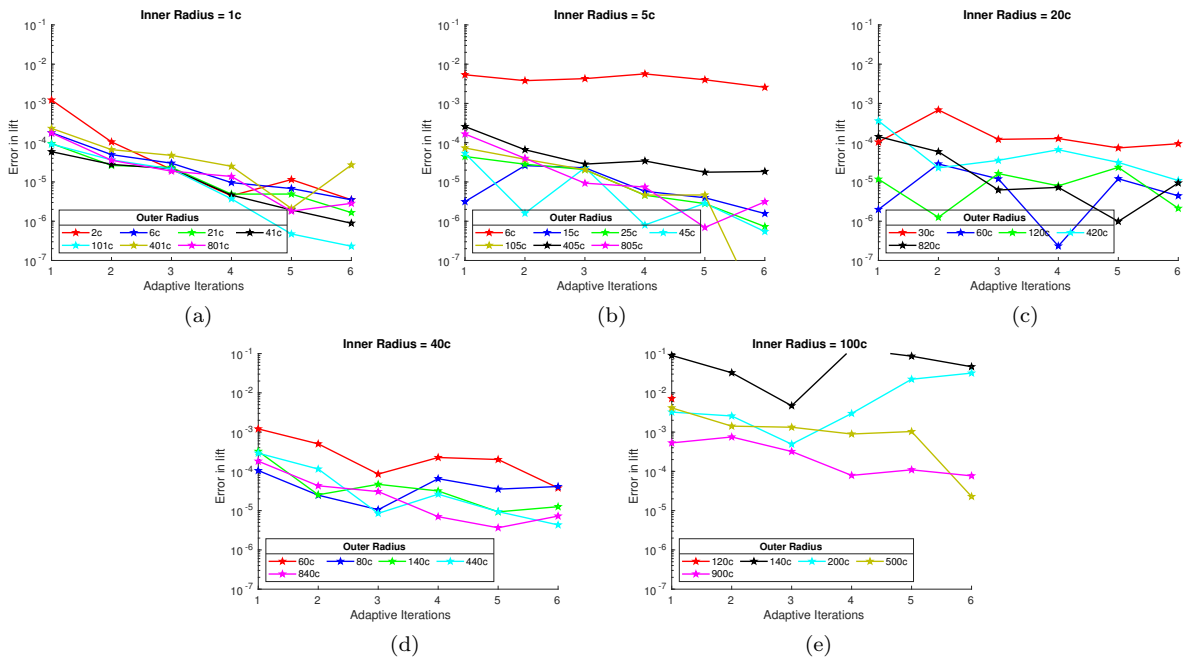
American Institute of Aeronautics and Astronautics

Cleared for Public Release on 8 November 2019. Case Number: 88ABW-2019-5482.

Figure 15. Error in lift generated by the airfoil in a laminar flow as a function of the adaptive iterations for the third mesh adaptation strategy.
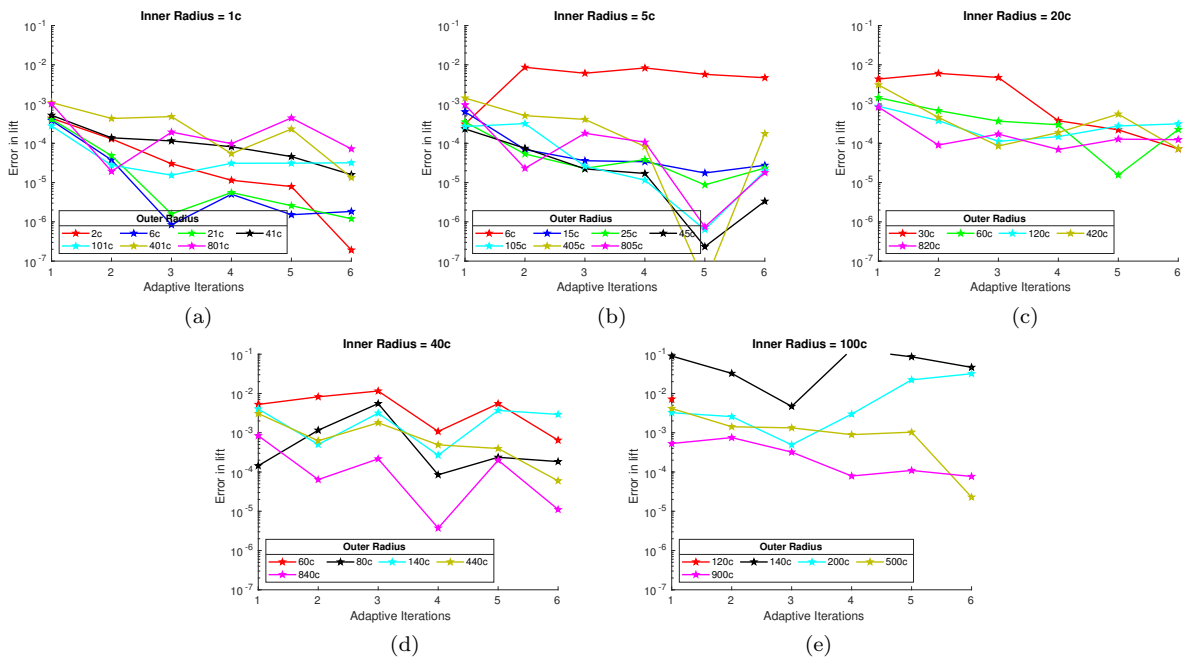

Figure 16. Error in lift generated by the airfoil in an inviscid flow as a function of the adaptive iterations for the first mesh adaptation strategy.

American Institute of Aeronautics and Astronautics

Cleared for Public Release on 8 November 2019. Case Number: 88ABW-2019-5482.
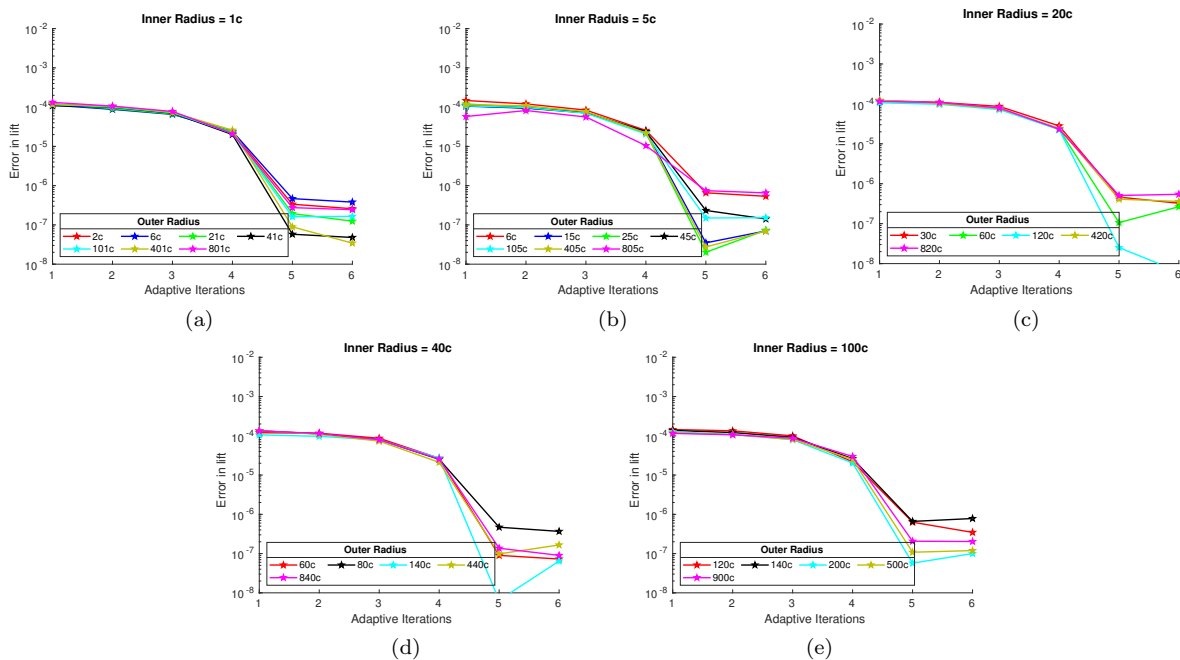
Figure 17. Error in lift generated by the airfoil in an inviscid flow as a function of the adaptive iterations for the second mesh adaptation strategy.
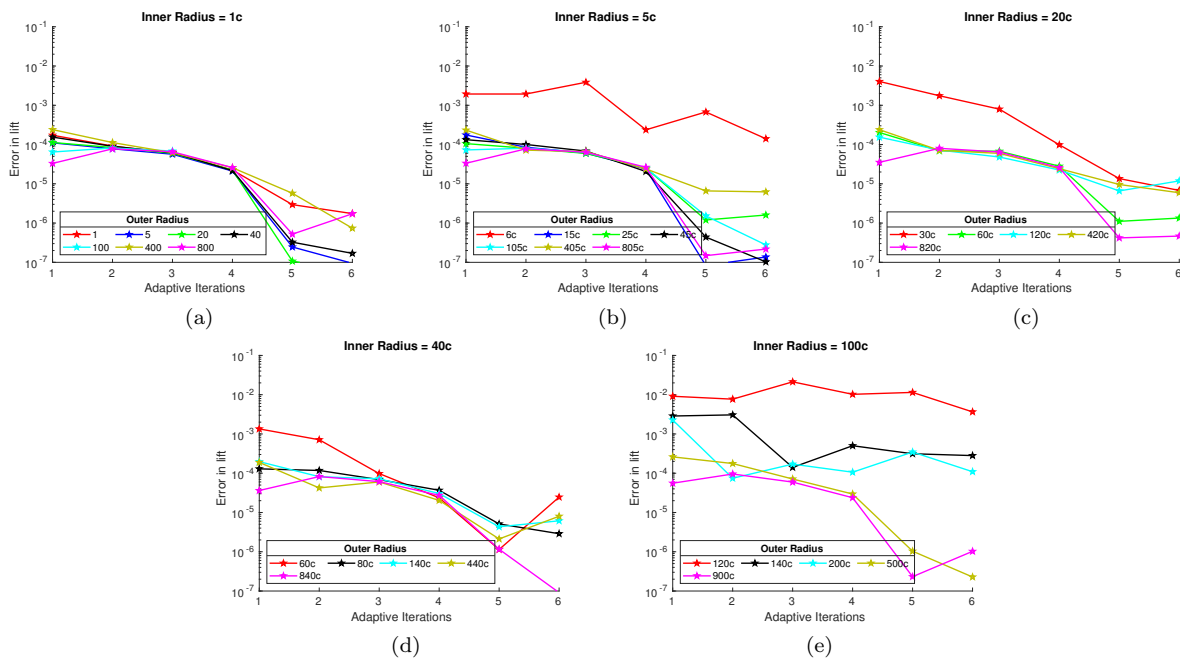

Figure 18. Error in lift generated by the airfoil in an inviscid flow as a function of the adaptive iterations for the third mesh adaptation strategy.

American Institute of Aeronautics and Astronautics

Cleared for Public Release on 8 November 2019. Case Number: 88ABW-2019-5482.

[9]Lesoinne, M. and Farhat, C., "Geometric conservation laws for flow problems with moving boundaries and deformable meshes, and their impact on aeroelastic computations," *Computer Methods in Applied Mechanics and Engineering*, Vol. 134, No. 1, 1996, pp. 71 – 90.

[10]Ojha, V., Fidkowski, K., and Cesnik, C. E. S., "High-Fidelity Coupled Fluid-Structure Interaction Simulations with Adaptive Meshing," *AIAA Aviation 2019 Forum*, 2019, p. 3056.

[11]Kast, S. M. and Fidkowski, K. J., "Output-based Mesh Adaptation for High Order Navier-Stokes Simulations on Deformable Domains," *Journal of Computational Physics*, Vol. 252, No. 1, 2013, pp. 468–494.

[12]Fidkowski, K. J., Oliver, T. A., Lu, J., and Darmofal, D. L., "p-Multigrid solution of high–order discontinuous Galerkin discretizations of the compressible Navier-Stokes equations," *Journal of Computational Physics*, Vol. 207, 2005, pp. 92–113.

[13]Fidkowski, K. J., "Output-Based Space-Time Mesh Optimization for Unsteady Flows Using Continuous-in-Time Adjoints," *Journal of Computational Physics*, Vol. 341, No. 15, July 2017, pp. 258–277.

[14]Fidkowski, K. J. and Darmofal, D. L., "Review of Output-Based Error Estimation and Mesh Adaptation in Computational Fluid Dynamics," *AIAA Journal*, Vol. 49, No. 4, 2011, pp. 673–694.

[15]Hecht, F., "BAMG: bidimensional anisotropic mesh generator," *User Guide. INRIA, Rocquencourt*, 1998.

[16]Venditti, D. A. and Darmofal, D. L., "Grid adaptation for functional outputs: application to two-dimensional inviscid flows," *Journal of Computational Physics*, Vol. 176, No. 1, 2002, pp. 40–69.

American Institute of Aeronautics and Astronautics
Cleared for Public Release on 8 November 2019. Case Number: 88ABW-2019-5482.